

Backscatter Differential Phase—Estimation and Variability

SILKE TRÖMEL

*Atmospheric Dynamics and Predictability Branch, Hans-Ertel-Centre for Weather Research,
University of Bonn, Bonn, Germany*

MATTHEW R. KUMJIAN

Advanced Study Program, National Center for Atmospheric Research, Boulder, Colorado*

ALEXANDER V. RYZHKOV

*Cooperative Institute for Mesoscale Meteorological Studies, University of Oklahoma, and
NOAA/OAR/National Severe Storms Laboratory, Norman, Oklahoma*

CLEMENS SIMMER

Meteorological Institute of the University of Bonn, Bonn, Germany

MALTE DIEDERICH

*Atmospheric Dynamics and Predictability Branch, Hans-Ertel-Centre for Weather Research,
University of Bonn, Bonn, Germany*

(Manuscript received 9 April 2013, in final form 11 June 2013)

ABSTRACT

On the basis of simulations and observations made with polarimetric radars operating at X, C, and S bands, the backscatter differential phase δ has been explored; δ has been identified as an important polarimetric variable that should not be ignored in precipitation estimations that are based on specific differential phase K_{DP} , especially at shorter radar wavelengths. Moreover, δ bears important information about the dominant size of raindrops and wet snowflakes in the melting layer. New methods for estimating δ in rain and in the melting layer are suggested. The method for estimating δ in rain is based on a modified version of the “ZPHI” algorithm and provides reasonably robust estimates of δ and K_{DP} in pure rain except in regions where the total measured differential phase Φ_{DP} behaves erratically, such as areas affected by nonuniform beam filling or low signal-to-noise ratio. The method for estimating δ in the melting layer results in reliable estimates of δ in stratiform precipitation and requires azimuthal averaging of radial profiles of Φ_{DP} at high antenna elevations. Comparisons with large disdrometer datasets collected in Oklahoma and Germany confirm a strong interdependence between δ and differential reflectivity Z_{DR} . Because δ is immune to attenuation, partial beam blockage, and radar miscalibration, the strong correlation between Z_{DR} and δ is of interest for quantitative precipitation estimation: δ and Z_{DR} are differently affected by the particle size distribution (PSD) and thus may complement each other for PSD moment estimation. Furthermore, the magnitude of δ can be utilized as an important calibration parameter for improving microphysical models of the melting layer.

*The National Center for Atmospheric Research is sponsored by the National Science Foundation.

Corresponding author address: Dr. Silke Trömel, Universität Bonn, Auf dem Hügel 20, 53121 Bonn, Germany.
E-mail: silke.troemel@uni-bonn.de

1. Introduction

Backscatter differential phase δ is one of the polarimetric variables that can be estimated from dual-polarization weather radar measurements. By definition, δ is the difference between the phases of horizontally and vertically polarized components of the wave caused by

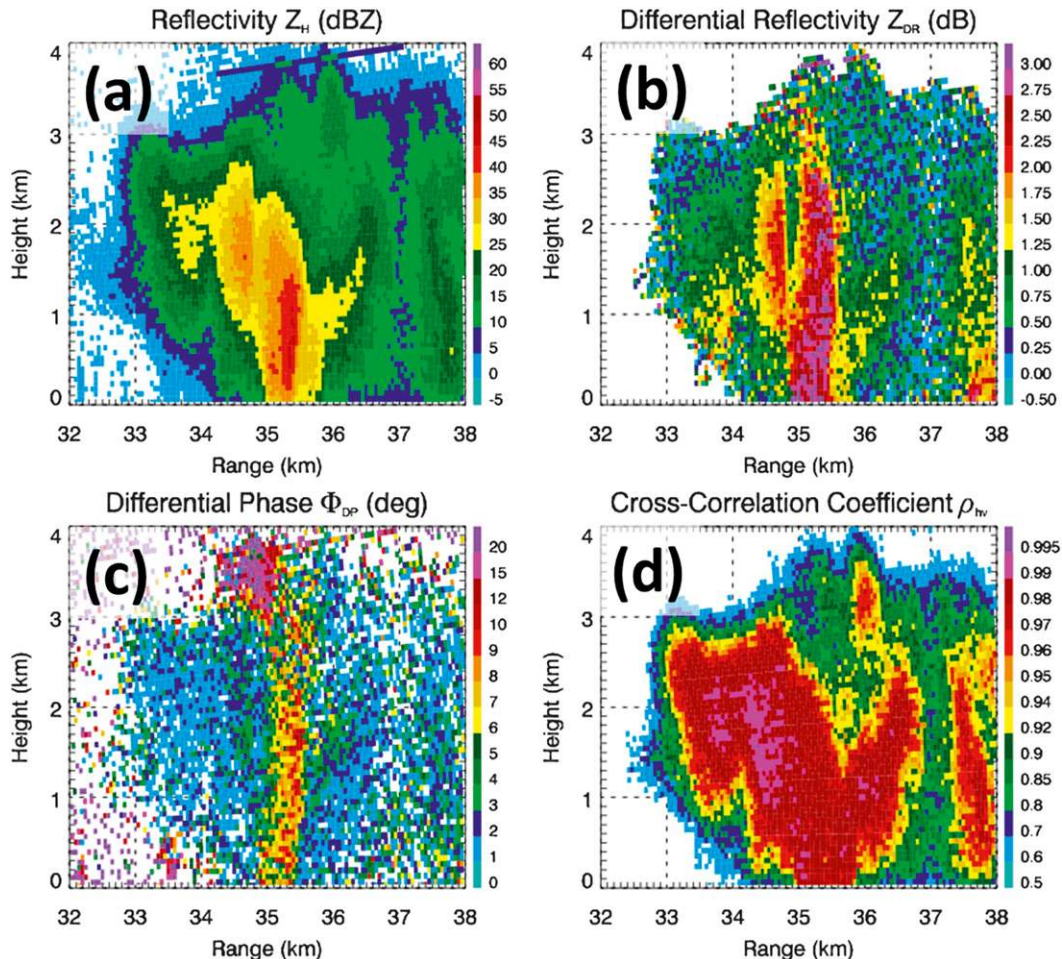


FIG. 1. Genuine RHI taken with 0.1° -elevation-angle spacing using the BoXPol X-band radar at 1424 UTC 22 Jun 2011 for (a) Z_H , (b) Z_{DR} , (c) Φ_{DP} , and (d) ρ_{hv} , showing evidence of differential phase upon backscattering in a column centered at about 35-km range from the radar. Note that the region of large Φ_{DP} values located between 3 and 4 km in height at a range of 34.5 km is associated with contamination from sidelobes and is not meteorological.

backscattering from objects within the radar resolution volume. It occurs when nonspherical hydrometeors are large enough relative to the radar wavelength such that scattering is in the Mie or so-called resonance regime.

The backscatter differential phase and its practical utilization are not well explored yet. Backscatter differential phase δ (measured in degrees) contributes to the total measured differential phase Φ_{DP} ($^\circ$), along with the propagation differential phase φ_{DP} ($^\circ$), which is determined by the radial profile of the specific differential phase K_{DP} ($^\circ \text{ km}^{-1}$) as

$$\Phi_{DP}(r) = \delta(r) + 2 \int_0^r K_{DP}(s) ds = \delta(r) + \varphi_{DP}(r). \quad (1)$$

Hence, contributions from the backscattered and propagation components of Φ_{DP} need to be separated before K_{DP} is estimated from the range derivative of the

remaining part of Φ_{DP} (i.e., φ_{DP}) and used for quantitative precipitation estimation. It has been recognized that accurate rainfall measurements using K_{DP} (particularly at X band) are contingent on the effectiveness of such a separation (e.g., Matrosov et al. 1999, 2002; Otto and Russchenberg 2011; Schneebeli and Berne 2012).

As an example of δ observed in rain, Fig. 1 presents a range–height indicator (RHI) scan taken on 22 June 2011 with the X-band polarimetric radar¹ at the University of Bonn in Germany (BoXPol). A prominent column of enhanced differential reflectivity Z_{DR} is observed in the core of the cell at a range of about 35 km. In this Z_{DR} column, Φ_{DP} values jump as high as 5° – 10°

¹For details of the dual-polarized X-band Doppler radars at Bonn (BoXPol) and Jülich (JuXPol, evaluated later), see Borowska et al. (2011).

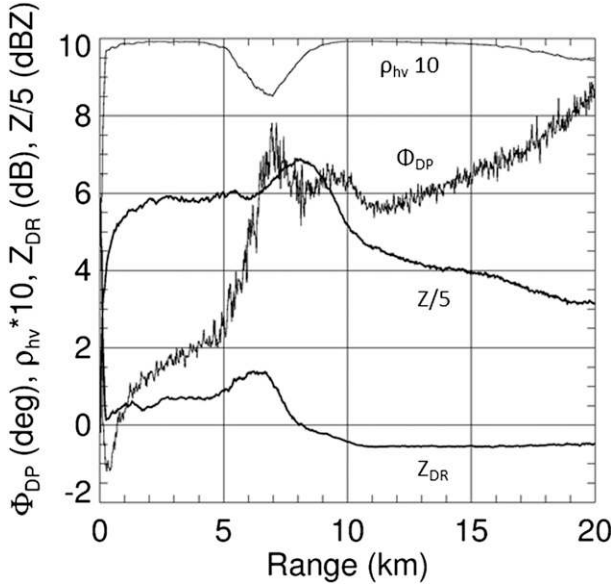


FIG. 2. Azimuthally averaged radial profiles of Φ_{DP} , Z_H (divided by 5), Z_{DR} , and ρ_{hv} (multiplied by 10) at elevation angle 7.0° within the melting layer, measured at X band by BoXPol at 2051 UTC 4 Dec 2011.

before returning to their background values (0° – 4°) on the far side of the core. Such clear nonmonotonic behavior in Φ_{DP} strongly suggests contributions from δ . The apparent “ δ bump” coincides with local increases in both Z_{DR} and reflectivity at horizontal polarization Z_H .

Resonance-sized wet snowflakes may also cause δ bumps in the melting layer of stratiform precipitation. A possible manifestation of δ in the melting layer is nonmonotonic radial profiles of Φ_{DP} through the layer. An example of such a perturbation in the mean radial profile of Φ_{DP} in a 7.0° -elevation plan position indicator (PPI) scan at X band is shown in Fig. 2, along with the corresponding azimuthally averaged radial plots of reflectivity Z , Z_{DR} , and cross-correlation coefficient ρ_{hv} . Zrnić et al. (1993) suggested that these kinds of perturbations are entirely related to δ and that the magnitude of the Φ_{DP} excursion can be used for the estimation of δ , as well as of the dominant (or maximal) size of wet snowflakes within the melting layer. Ryzhkov and Zrnić (1998) and Ryzhkov (2007) provide an alternative explanation for such perturbations of Φ_{DP} profiles and attribute at least part of it to effects of nonuniform beam filling (NBF). The relative contributions of NBF and δ to the observed signatures in the melting layer remain to be clarified.

Clear manifestations of δ are frequently observed in rain at X and C bands, as well as in wet snow and melting hail at X, C, and S bands. Systematic studies of δ with respect to hydrometeor types are still missing, however, partly because of the difficulty in accurately estimating δ , particularly in the melting layer and in hail. Under

such conditions, Φ_{DP} is often very noisy because of significant reductions of ρ_{hv} , which are commonly associated with enhanced δ (Balakrishnan and Zrnić 1990).

The goal of this study is to develop methods to estimate δ for precipitation that contains different types of hydrometeors, as well as to explore its variability. The next section provides a theoretical background for δ , including simulations (of δ at S, C, and X bands for liquid and mixed-phase particles) that are based on large disdrometer datasets collected in Oklahoma and Germany and on microphysical and polarimetric models for melting snow and hail. New methods for estimating δ in rain and in the melting layer are presented in section 3. Results of δ estimation using polarimetric radars operating at X, C, and S bands are presented in section 4. Section 5 is a discussion of potential applications of δ , and the main conclusions are summarized in section 6.

2. Theoretical background

A general expression for δ can be obtained following, for example, the derivations in Ryzhkov (2001) and Ryzhkov et al. (2011):

$$\delta = \arg(\langle S_{hh}^* S_{vv} \rangle) = \arg[\langle |s_b|^2 \rangle + \langle |s_a|^2 \rangle A_3 - \langle s_b^* (s_b - s_a) \rangle A_1 - \langle s_b (s_b^* - s_a^*) \rangle A_2]. \quad (2)$$

In this equation, $S_{hh,vv}$ are the elements of the scattering matrix, $s_{a,b}$ are the complex scattering amplitudes of individual spheroidal hydrometeors along their major and minor axes (b and a , respectively), and A_{1-3} are angular moments defined in Ryzhkov et al. (2011) as

$$A_1 = \langle \sin^2 \psi \cos^2 \alpha \rangle, \quad A_2 = \langle \sin^2 \psi \sin^2 \alpha \rangle, \quad \text{and} \quad A_3 = \langle \sin^4 \psi \cos^2 \alpha \sin^2 \alpha \rangle, \quad (3)$$

where α is the particle canting angle within the polarization plane and ψ is the angle between the direction of propagation and the symmetry axis of the hydrometeor. In Eq. (2), the angular brackets indicate the ensemble average over particle sizes, shapes, and dielectric constants. For ensembles of hydrometeors with the same orientation, $A_1 = 1$, $A_2 = A_3 = 0$, and Eq. (2) reduces to

$$\delta = \arg(\langle s_b^* s_a \rangle). \quad (4)$$

For fully random orientation of particles A_1 is equal to A_2 and the value of $\langle S_{hh}^* S_{vv} \rangle$ in Eq. (2) becomes real, meaning that $\delta = 0$. Hence, δ decreases as hydrometeors become more randomly oriented.

a. Backscatter differential phase of raindrops

The backscatter differential phase of raindrops is computed in this study by assuming the shape–diameter

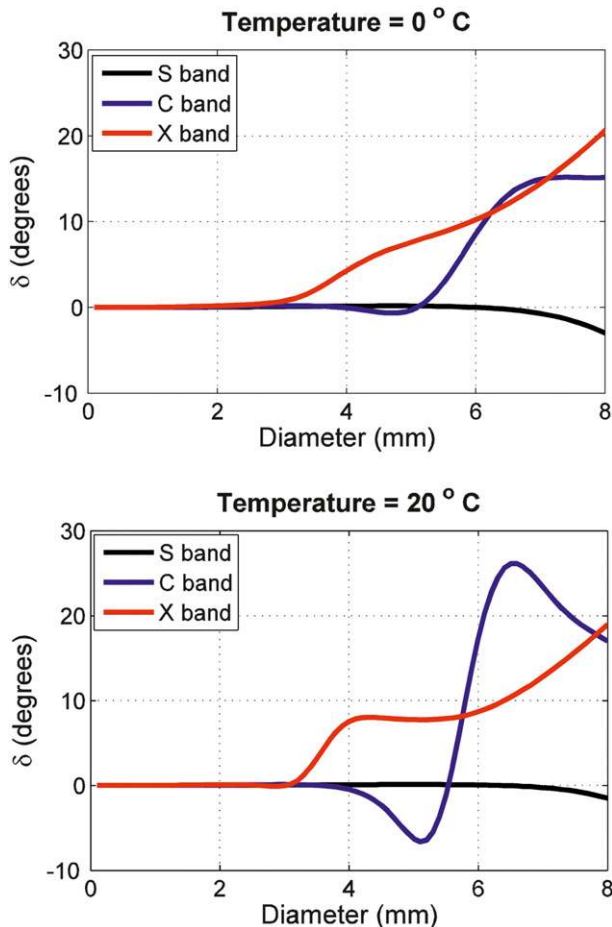


FIG. 3. Backscatter differential phase δ as a function of equivolume raindrop diameter for different wavelengths and temperatures. Wavelengths λ are 11.0 (S band), 5.45 (C band), and 3.2 (X band) cm.

relation specified by Brandes et al. (2002; corrected in 2005), with a 10° canting-angle distribution width following Ryzhkov et al. (2011). The magnitude of δ in rain strongly depends on wavelength and also depends on temperature (Fig. 3). At S band, δ is usually insignificant for rain, whereas it can exceed 20° at C and X bands for very large drops. The magnitude of δ is small for drop diameters below 4.5 mm at C band and below 2.5 mm at X band. Notable is the nonmonotonic behavior of δ as a function of raindrop size at higher temperatures at C band. This behavior is a direct consequence of resonance scattering by raindrops with diameters larger than 5 mm. The resonance effects are weaker at X band than at C band.

The Rayleigh formulas for the scattering amplitudes s_a and s_b (e.g., Doviak and Zrnić 1993) can be used in Eq. (2) to compute δ only if raindrops are very small, for which δ gets close to zero and loses its diagnostic value. The inappropriateness of the Rayleigh formulas

for estimating δ follows from its dependence on the imaginary parts of the scattering amplitudes, which are not well approximated by the Rayleigh solution. Therefore, in practice more sophisticated scattering calculations (such as the T-matrix method; e.g., Mishchenko 2000) must be employed to compute δ .

To investigate the natural variability of δ in rain, a disdrometer dataset of more than 47 000 drop size distributions (DSDs) measured with a 2D video disdrometer in central Oklahoma was used to simulate δ in rain at S, C, and X bands. The scatterplots of δ versus Z_H displayed in Fig. 4 are computed for a temperature of 20°C . It is notable that δ is usually higher at X band than at C band, but values approaching 30° can be observed for a small fraction of rain DSDs containing resonance-sized drops at C band.

Other authors have already noted a relation between δ and Z_{DR} in rain. For example, Otto and Russchenberg (2011) suggested a best-fit relationship $\delta = Z_{DR}^{1.8}$, with δ in degrees and Z_{DR} in decibels, that is based on scattering computations at X band applied to a set of 1500 DSDs. Schneebeli and Berne (2012) confirm their results with a similar best-fit power law:

$$\delta = 0.632 Z_{DR}^{1.71}, \quad (5)$$

where again δ is in degrees and Z_{DR} is in decibels. The authors claim that the difference between the two Z_{DR} – δ relations predominantly stems from disregarded temperature effects. To investigate the temperature dependence, the Oklahoma disdrometer dataset is used to calculate Z_{DR} and δ at 0° and 30°C . Figure 5a summarizes these calculations, which clearly reflect the temperature impact on the Z_{DR} – δ relationship. For comparison, the best-fit power law $\delta = Z_{DR}^{1.8}$ suggested by Otto and Russchenberg (2011) for the temperature range between 1° and 25°C is included in Fig. 5a. Remarkable differences are evident for the wide temperature range considered. We conclude that for higher temperatures one has to expect larger exponents and significantly larger δ for a given Z_{DR} . Possible climatological impacts on Z_{DR} – δ relations that are due to different typical DSDs are investigated in a repetition of the above calculations for measurements from a Particle Size and Velocity (PARSIVEL) disdrometer in Bonn, Germany, covering the time period of August 2007–January 2010 (Fig. 5b). It is obvious that the Z_{DR} – δ scatterplots retrieved from both sites are consistent; thus, the overwhelming part of the variability is apparently related to raindrop temperature variation while the impact of differences in DSDs, at least for those typical for Oklahoma and Bonn, seems to be of secondary importance.

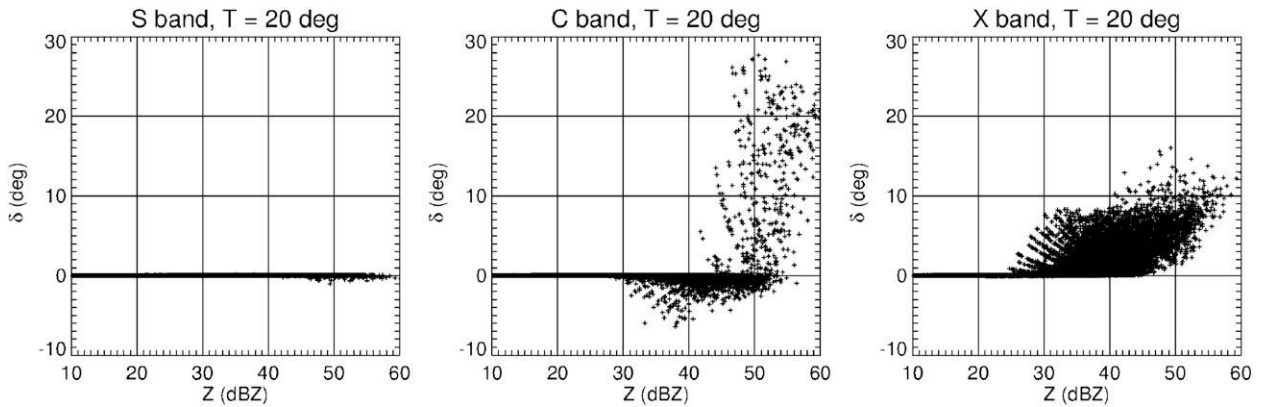


FIG. 4. Scatterplots of δ vs Z_H in rain simulated from disdrometer data at S band ($\lambda = 11.0$ cm), C band ($\lambda = 5.45$ cm), and X band ($\lambda = 3.2$ cm) for $T = 20^\circ\text{C}$.

Although disdrometers provide a good measure of the natural variability of temporally averaged DSDs, transient phenomena including size sorting are not well sampled by them (e.g., Cao et al. 2008). Thus, δ – Z_{DR} relations that are based on disdrometer data may not always be appropriate for polarimetric radar retrievals because they do not reflect certain phenomena. Ongoing size sorting is, however, well observed by polarimetric radars through differential reflectivity Z_{DR} (e.g., Kumjian and Ryzhkov 2012). To mimic the potential impact of size sorting on the δ – Z_{DR} relation, we progressively truncated the small-drop-size end of the spectrum (Fig. 6). It is obvious that size sorting tends to produce steeper slopes of the δ – Z_{DR} relation such that, for a given value of Z_{DR} , smaller values of δ are possible. Thus, disdrometer-derived δ – Z_{DR} relations may overestimate δ in cases of

ongoing size sorting, which might happen beneath developing convection, at the leading edge of linear convective systems, and in the Z_{DR} arc of supercell storms (Kumjian and Ryzhkov 2008, 2009).

b. Backscatter differential phase of dry frozen and mixed-phase hydrometeors

Backscatter differential phase δ in dry frozen hydrometeors is usually very low because of the small imaginary part of the ice dielectric constant at S, C, and X bands (Balakrishnan and Zrnić 1990; Ryzhkov et al. 2011). Thus, δ is negligible for most ice hydrometeor types, including snow, crystals, and graupel, at these wavelengths. Large dry hailstones with nonspherical shapes may, however, have noticeable δ that is highest at X band. Wet hailstones can exhibit much higher δ , and

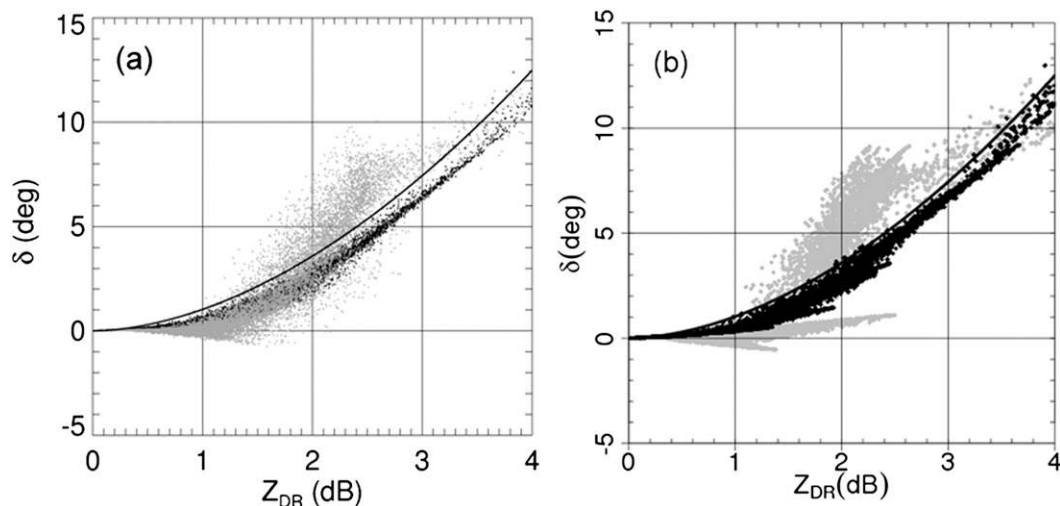


FIG. 5. Scatterplots of δ vs Z_{DR} in rain at X band as revealed from simulations using (a) the Oklahoma disdrometer dataset and (b) PARSIVEL measurements in Bonn. Black dots correspond to temperatures at 0°C , and gray dots are for temperatures at 30°C . The solid lines depict the dependence $\delta = Z_{\text{DR}}^{0.8}$.

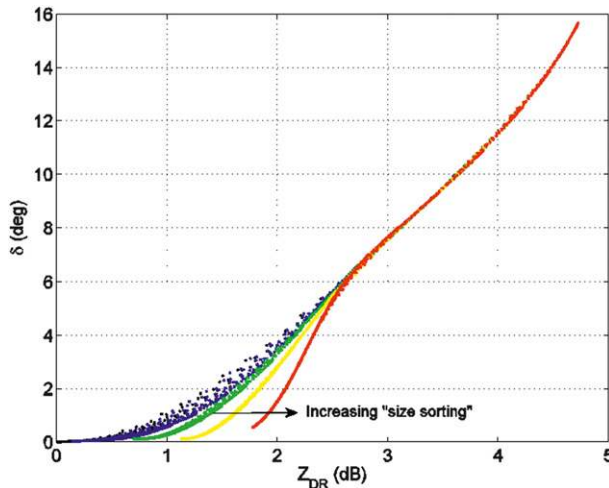


FIG. 6. Simulated δ - Z_{DR} pairs for DSDs undergoing progressively more size sorting as colors change from black to blue, green, yellow, and red. Calculations are performed at X band, for 20°C raindrops.

even negative values might occur at about 5.8 cm for S band, 2.9 cm for C band, and 1.7 cm for X band (e.g., Aydin et al. 1991).

To better understand the complex behavior of δ in realistic hydrometeor populations, we first simulate vertical profiles of δ in melting hail mixed with rain for different size distributions of graupel and hail at the freezing level. The thermodynamic part of the model for melting hail is taken from Rasmussen and Heymsfield (1987), and the radar scattering simulation part is described in Ryzhkov et al. (2011, 2013a,b). Melting and shedding are treated explicitly, but no collisions between particles are taken into account. In our simulations we prescribe a biexponential size distribution of graupel/hail at a freezing level of 4 km according to

$$N(D) = N_g \exp(-\Lambda_g D) + N_h \exp(-\Lambda_h D), \quad (6)$$

where subscripts g and h indicate graupel and hail, respectively. The size distribution of hail aloft is truncated at the maximal initial hail diameter D_{max} . The hydrometeors are modeled as oblate spheroids with aspect ratios and orientations that depend on the mass water fraction as specified in Ryzhkov et al. (2011). A T-matrix code, which considers two-layer spheroids, is utilized for computing δ for ice spheroids coated with liquid water. Dielectric constants of water and ice are determined following Ray (1972). Here, we compare results for 1) no hail, 2) small hail, 3) moderate hail, and 4) large hail at S, C, and X bands. The size distribution parameters for graupel and hail aloft are specified in Ryzhkov et al. (2013a) and are listed here in Table 1. Small hail completely

TABLE 1. Parameters of size distributions of dry hail at the freezing level.

Hail size	Λ_h (mm ⁻¹)	N_h (m ⁻³ mm ⁻¹)	D_{max} (mm)
No hail	—	0	—
Small hail	0.99	$200\Lambda_h^{4.11}$	14
Moderate hail	0.42	$400\Lambda_h^{4.11}$	24
Large hail	0.27	$800\Lambda_h^{4.11}$	35

melts before reaching the surface. The “graupel” part of the size distribution [see Eq. (5)] was parameterized either as close to the Marshall–Palmer distribution with $N_g = 8000$ m⁻³ mm⁻¹ and $\Lambda_g = 1.6$ mm⁻¹ or as a “flatter” distribution, which we consider to be more typical for hail-bearing storms, with $N_g = 1500$ m⁻³ mm⁻¹ and $\Lambda_g = 1.1$ mm⁻¹. Vertical profiles of δ computed for all four cases at S, C, and X bands are displayed in Fig. 7. Small hail is assumed to be completely melted by 4 km below the melting layer while moderate and large hail have maximal solid diameters at the surface equal to 19 and 30 mm, respectively. Although the intrinsic δ of individual hailstones at resonance size can be very high, the calculations displayed in Fig. 7 show that their contribution to the magnitude of δ for any realistic size distributions of melting hailstones mixed with rain is relatively small. The resulting δ can be comparable to or even lower than δ for pure rain at C and X bands. Only at S band does δ in melting hail increase monotonically with size over the modeled range.

Next, we simulate δ within the melting layer by using the microphysical and scattering model for melting snow that was described by Giangrande (2007) and Ryzhkov et al. (2013a). An example of resulting vertical profiles of δ along with Z_H and Z_{DR} is presented in Fig. 8 for unrimed snow. It is assumed that the size distribution of dry snowflakes aloft is such that the resulting rain DSD below the melting layer follows the Marshall–Palmer distribution with a rainfall rate of 5 mm h⁻¹. The thermodynamic part of the model is consistent with the model utilized by Zawadzki et al. (2005) and assumes that mixed-phase particles do not interact with each other and that wet snowflakes do not aggregate. As a result, the simulated values of δ are relatively small and barely exceed 4° at all three wavelengths. Taking aggregation into account in the model is challenging, but there are clear indications that the magnitude of δ can be significantly higher in the presence of aggregation, as will be shown later (see section 5).

3. Estimating backscatter differential phase

a. Estimation of δ in rain

Few studies exist that explicitly address detection and quantification of δ in data processing. A simple

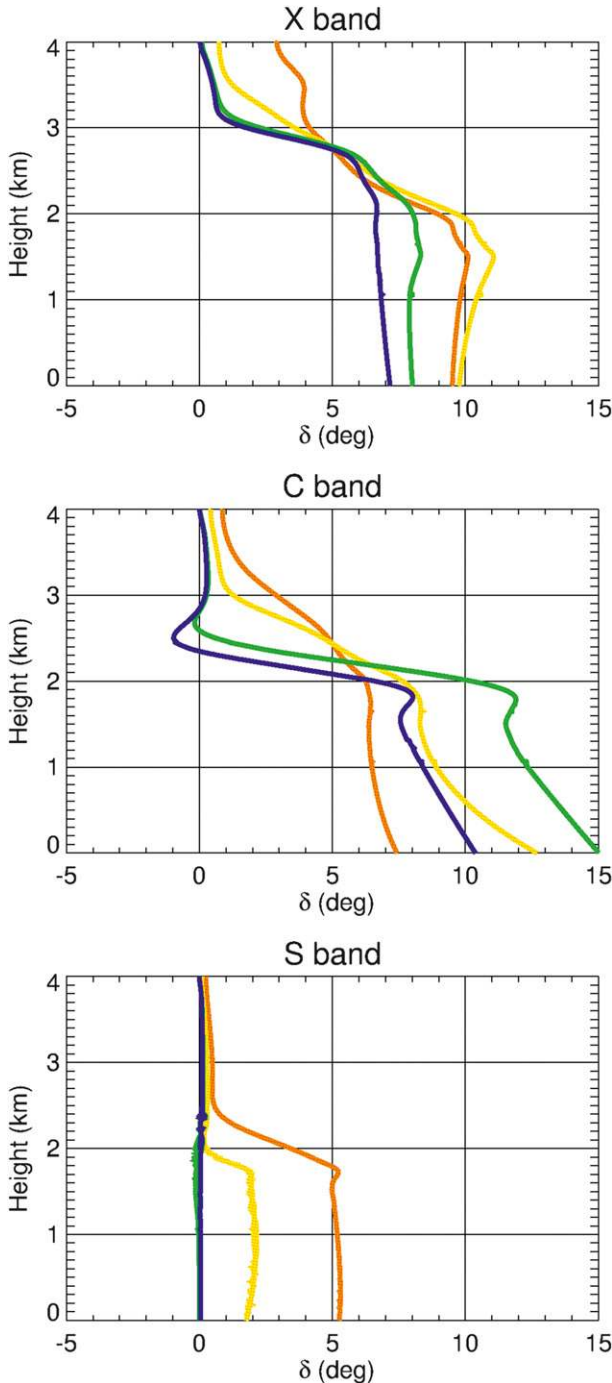


FIG. 7. Vertical profiles of backscatter differential phase for the cases of no hail (blue curves), small hail (green curves), moderate hail (yellow curves), and large hail (orange curves) at S, C, and X bands. The parameters of the model of melting hail are summarized in Table 1.

moving-average filter with ensuing least squares fit is often used to reduce fluctuations before estimating K_{DP} . This simple procedure at least partly eliminates the δ bumps below the cutoff frequency of the filter. This

method also allows estimation of δ signatures by subtracting the filtered from the raw measured Φ_{DP} if—and this is the drawback of the method—the filter characteristics are appropriate for the scale of the δ bumps. If significant δ extends over a great enough range, a single filtering will not suppress this δ variation. If significant δ effects extend over ranges that exceed the stop band of the filter, the leftover δ might corrupt K_{DP} estimates. A filter with a lower cutoff frequency comes, however, with the price of lower range sensitivity of K_{DP} estimates. Hubbert and Bringi (1995) combined a finite-impulse response filter with an iterative procedure: within each iteration, a new best estimate of the propagation range profile (called Ψ_c) is constructed by selecting data points from both the raw (measured) Φ_{DP} and its filtered version, as determined by a threshold. Large deviations of the raw Φ_{DP} range profile from the filtered range profile were considered to be potentially due to δ . The threshold is set according to the expected standard deviation σ of the raw range profile Φ_{DP} . Thresholds of $1.25\text{--}2 \times \sigma$ were found to give good results. The authors claim that this method detects δ bumps extending over longer ranges while avoiding low cutoff frequencies. Such filters would also eliminate the more subtle mean variations and result in a decrease of the range sensitivity of the K_{DP} estimates. The outcome, however, still depends on both the cutoff frequency of the filter and the decision-threshold value used to construct the iterated differential propagation phase range profile.

Otto and Russchenberg (2011) suggested a technique for estimating δ in rain at X band, with the assumption that δ is closely correlated with Z_{DR} . Then the difference in differential phase between two range bins $r_b > r_a$, defined as $\Delta\Phi_{DP} = \Phi_{DP}(r_b) - \Phi_{DP}(r_a)$, that have the same nonattenuated Z_{DR} [i.e., $Z_{DR}(r_a) = Z_{DR}(r_b)$] can only be caused by a difference in the propagation phase φ_{DP} between both range bins. However, $\Delta\Phi_{DP}$ may still contain significant residual δ effects caused by microphysical variations, statistical fluctuations, and imprecise corrections for differential attenuation. Such residuals in $\Delta\Phi_{DP}$ are reduced by testing each combination of two range bins along a radar ray to determine whether $|Z_{DR}(r_b) - Z_{DR}(r_a)|$ is below a predefined threshold, c_{ZDR} . As a result, for one radar ray, a set of $\Delta\Phi_{DP}$ is produced for different ray segments. These $\Delta\Phi_{DP}$ are then distributed among the corresponding range bins that have contributed to the phase shift, such that, at each range bin, a number of $K_{DP}^{(i)}$ are available. The K_{DP} estimate at a range bin is then determined as the average value of all K_{DP} values resulting from the procedure. The δ can then be identified as the difference between the total measured differential phase Φ_{DP} and the estimated differential propagation phase φ_{DP} .

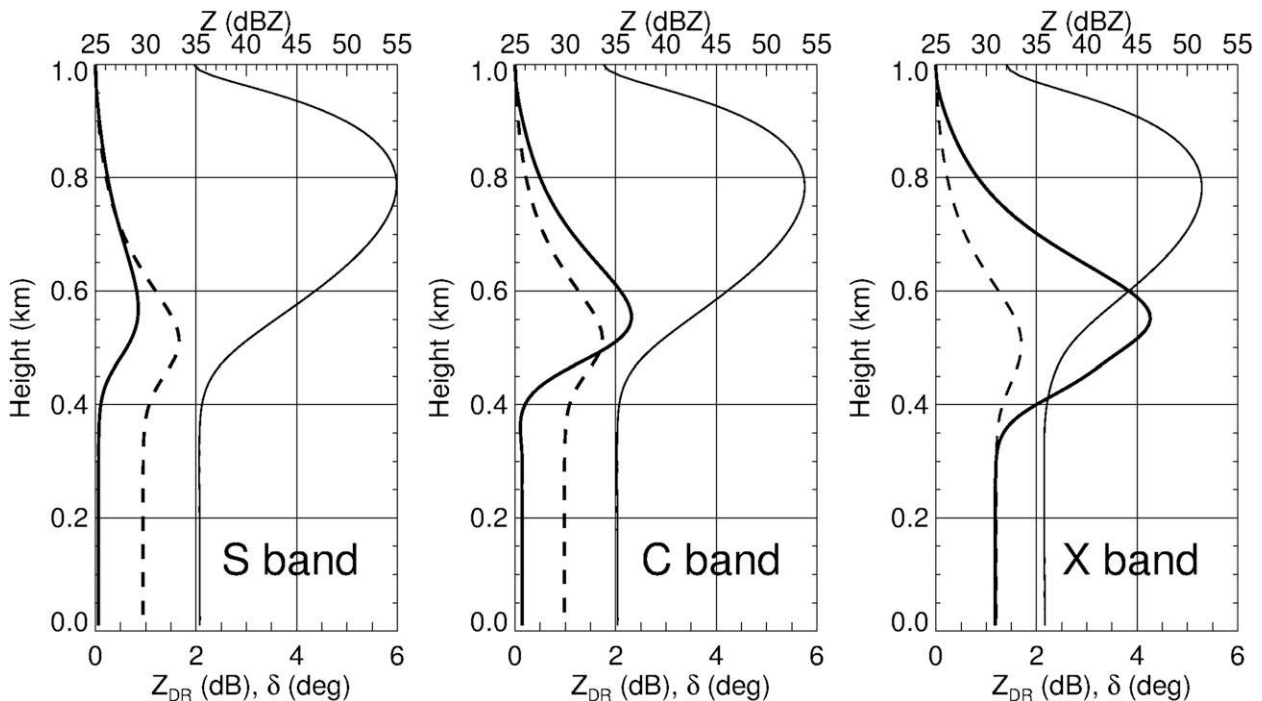


FIG. 8. Simulated vertical profiles of Z_H , Z_{DR} , and δ within the melting layer at S, C, and X bands. The freezing level is at 1 km; the temperature lapse rate is 6.5°km^{-1} , relative humidity is 100%, and the rain rate near the surface is 5 mm h^{-1} . Thin solid curves depict Z_H , the dashed lines show Z_{DR} , and the thick solid lines represent δ .

Schneebeli and Berne (2012) developed an extended Kalman filter framework to derive a consistent set of polarimetric variables. The method exploits the redundancy caused by the close links between the polarimetric moments for optimized estimates of attenuation-corrected Z and Z_{DR} , as well as K_{DP} , φ_{DP} , and δ . The exploited functional relationships among polarimetric moments still contain parameters that depend on the DSD, however. They use, for example, the δ - Z_{DR} relation in Eq. (5). This relation is based on calculations with an assumed gamma function DSD (Ulbrich 1983); this relation is only valid for a narrow set of conditions, however.

We suggest an alternative method to estimate δ in pure rain that combines a modified “ZPHI” method (Testud et al. 2000) with a slightly modified version of the self-consistent method with constraints proposed by Bringi et al. (2001). Both methods only assume a power-law relation between specific attenuation A (dB km^{-1}) and nonattenuated reflectivity Z (usually Z_H is used, in logarithmic units),

$$A = \beta Z^b, \quad (7)$$

and a quasi-linear relationship between A and K_{DP} ($^\circ\text{km}^{-1}$),

$$A = \alpha K_{DP}^c, \quad (8)$$

with constants β , b , α , and c , where c is close to unity in the considered range interval. In addition, an external constraint (see below) that is determined by the total span of measured Φ_{DP} along the ray is used. Within this framework, it is possible to use the ZPHI method to derive the radial profile of specific attenuation $A(r)$ from the attenuated reflectivity $Z_a(r)$ (Testud et al. 2000). The constraint used herein is the cumulative attenuation from r_1 to r_2 , which must be consistent with the total change of φ_{DP} over this range interval. Because of the full flexibility in the choice of the integration bounds, it is generally possible to select them where δ is small enough to be neglected (i.e., $\Delta\Phi_{DP} = \Delta\varphi_{DP}$). Once $A(r)$ at each range is calculated according to the ZPHI algorithm, a “calculated” radial profile of differential propagation phase ($\varphi_{DP}^{\text{cal}}$) can be determined as

$$\varphi_{DP}^{\text{cal}}(r, \alpha; b) = 2 \int_{r_1}^r \frac{A(s; \alpha; b)}{\alpha} ds. \quad (9)$$

The self-consistent method of Bringi et al. (2001) searches for an optimal α by matching the calculated $\varphi_{DP}^{\text{cal}}$ and the measured Φ_{DP} . For our analysis, we slightly modify the

method such that both α and b are optimized to yield the smallest absolute difference:

$$\min_{\alpha, b} \Delta\varphi = \sum_{i=1}^N |\varphi_{\text{DP}}^{\text{cal}}(r_i; \alpha; b) - \Phi_{\text{DP}}(r_i)|, \quad (10)$$

where N is the number of range bins over which α and b are assumed to be constant. Park et al. (2005) found that α varied from 0.139 to 0.335 dB (°)⁻¹ and b varied from 0.76 to 0.84 at X band; thus, the optimal pair of (α , b) is selected on the basis of Eq. (10) by considering all possible combinations of the two within the intervals derived by Park et al. (2005), using 0.01 increments. A drawback of our method is that α and b depend on both DSD and temperature and therefore are functions of range. For practical applications, this necessitates a segmentation of each ray into small intervals for which the parameters can be considered to be constant (Le Bouar et al. 2001), which might conflict with the requirement that the intervals must be large enough so that $\Delta\varphi_{\text{DP}}$ can be measured reliably. For example, in areas of reduced ρ_{hv} the measured Φ_{DP} often becomes nonmonotonic and the identification of valid intervals becomes difficult and subjective. In this paper we test two modifications of the ZPHI method:

- 1) For practical reasons α and b are considered to be constant throughout the entire PPI scan (i.e., N is equal to 1000 bins in a ray times 360 for 1° radial resolution); the values are determined by the best estimates on the basis of the modified self-consistent method introduced above. This also includes that the segmentation of each ray into smaller intervals is avoided and the total span of measured Φ_{DP} along the ray is used: $\Delta\Phi_{\text{DP}} = \Delta\varphi_{\text{DP}}$.
- 2) The reflectivity at vertical polarization $Z = Z_V$ is used as input to the ZPHI method instead of Z_H because of lower attenuation at vertical polarization.

Once the smoothed differential propagation phase φ_{DP} is derived, δ is then obtained by propagation, subtracting φ_{DP} from the measured raw Φ_{DP} .

b. Estimation of δ in the melting layer

Measured Φ_{DP} routinely exhibits characteristic “bumps” also within the melting layer that may be associated with either δ or with NBF (see section 2b). Azimuthal averaging of Φ_{DP} data can be used to suppress fluctuations of Φ_{DP} caused by a reduction of ρ_{hv} within the melting layer, to separate effects of δ and K_{DP} , and to minimize the impact of NBF. It is recommended to use higher elevation angles (i.e., $\geq 7^\circ$). At higher elevations the forward propagation contribution to the differential phase is reduced, leading to increasingly “clean” δ

without contamination from K_{DP} . The forward-propagation part of Φ_{DP} is proportional to the product of K_{DP} and slant propagation path within the melting layer, which decreases with elevation, whereas δ is a local parameter and is not a path integral. In addition, azimuthal averaging is more efficient at higher elevations because the melting layer appears more uniform horizontally at smaller spatial scales. Also, NBF effects are smaller at higher elevations.

To separate effects of δ and NBF, the vertical gradients of azimuthally averaged Z_H and Φ_{DP} can be used at the elevation angle where the measurement is taken. For illustration we use the measurement at 7.0° displayed in Fig. 2 and examine the differences in the average radial dependencies of Z_H and Φ_{DP} at slightly higher/lower elevation angles θ (8.1° and 5.7°, respectively; see Figs. 9a,b). Note that all 360° are used to generate the averaged profiles. The NBF-induced bias of Φ_{DP} is then estimated from the product of the vertical gradients of Z and Φ_{DP} according to the formula

$$\Delta\Phi_{\text{DP}} = 0.02\Omega^2 \frac{d\Phi_{\text{DP}}}{d\theta} \frac{dZ_H}{d\theta}, \quad (11)$$

from Ryzhkov (2007), where Ω denotes the radar beamwidth in degrees. The radial plot of $\Delta\Phi_{\text{DP}}$ (Fig. 9c) shows that for this case the magnitude of the Φ_{DP} perturbation caused by NBF effects is within 0.1°. In this case NBF effects can consequently be neglected, and the disturbance of the Φ_{DP} profile is almost entirely due to δ . In this example, δ varies from 0° to 3° within the melting layer. The maximal value of azimuthally averaged δ along range is observed at the range (or height) at which ρ_{hv} is minimal.

In cases of uniform stratiform precipitation, all 360° can be averaged, and a maximum value of azimuthally averaged δ along range is subsequently estimated. Values of Φ_{DP} just above and below the melting layer are connected with a straight line (the vertical profile that would be expected as a result of K_{DP} only), and the difference between the actual average profile of Φ_{DP} and the straight line is used to derive the maximal azimuthally averaged δ . The included assumption of constant K_{DP} within the melting layer is uncritical at higher elevations because of the short integration path within the melting layer. Otherwise, an azimuthal sector containing subjectively identified uniform brightband characteristics is averaged. To estimate how much azimuthal averaging is needed, the standard error of the differential phase Φ_{DP} estimate (in degrees) determined as

$$\text{SD}(\Phi_{\text{DP}}) = 30.3 \left(\frac{\rho_{\text{hv}}^{-2} - 1}{\sigma_{\text{vn}} M} \right)^{1/2} \quad (12)$$

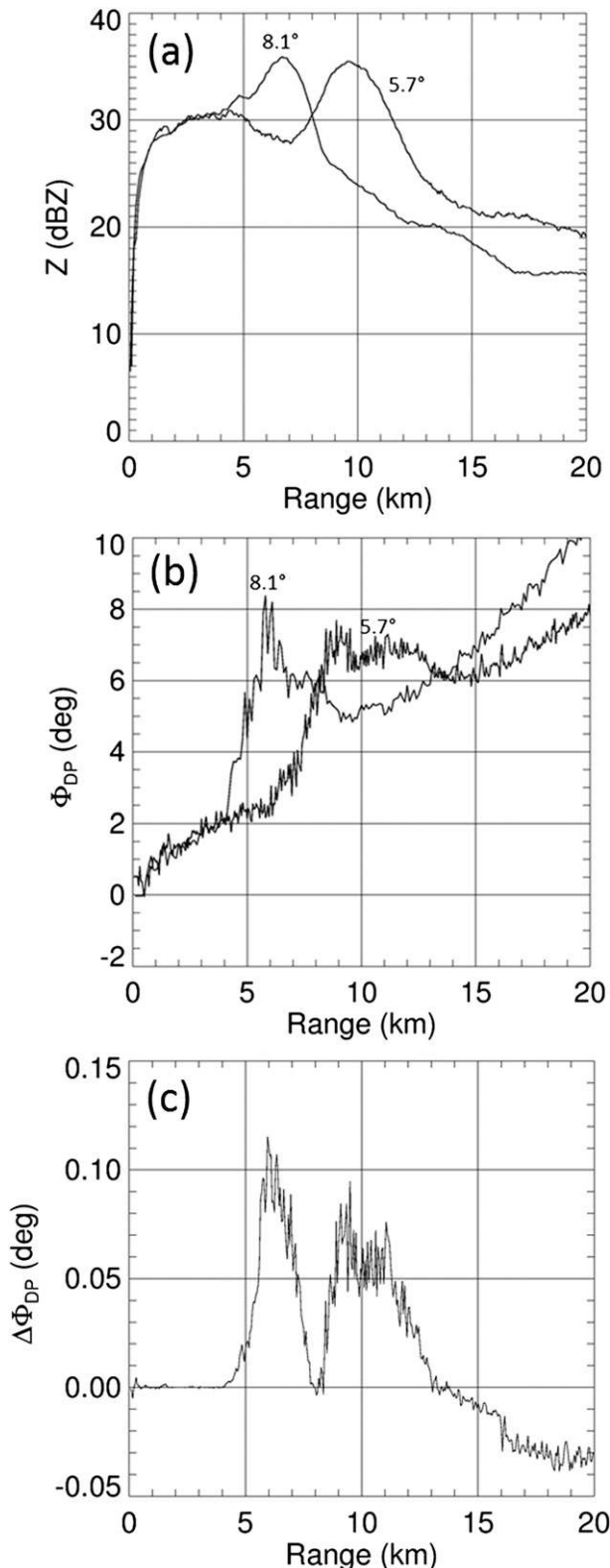


FIG. 9. Range profiles of azimuthally averaged (a) Z_H and (b) Φ_{DP} at elevation angles 8.1° and 5.7° . (c) Range profile of estimated Φ_{DP} bias caused by NBF at elevation angle 7.0° .

(e.g., Melnikov 2004), with $\sigma_{vn} = 4\sigma_v T/\lambda$, Doppler spectrum width σ_v , pulse repetition period T , radar wavelength λ , cross-correlation coefficient ρ_{hv} , and number of pulses M , can be considered. In pure rain or pure snow, the cross-correlation coefficient is very high (0.98–0.99) and $SD(\Phi_{DP})$ is small. Within the melting layer, ρ_{hv} can vary from 0.8 to 0.97 and statistical variations of Φ_{DP} may become so overwhelming that δ cannot be reliably measured on a radial basis. After averaging over N azimuths, the standard error of Φ_{DP} is reduced by a factor $N^{1/2}$, if horizontal uniformity is assumed. If we assume a worst-case scenario at X band when $\rho_{hv} = 0.8$, then Eq. (12) would yield $SD(\Phi_{DP}) = 5.4^\circ$ for $\sigma_v = 3 \text{ m s}^{-1}$, $T = 10^{-3} \text{ s}$, $\lambda = 3.2 \text{ cm}$, and $M = 48$. Averaging over a whole azimuthal scan (360 radials) would reduce $SD(\Phi_{DP})$ to 0.3° , which is more than sufficient. Hence, depending on the magnitude of ρ_{hv} within the melting layer, the number of radials to be averaged can be significantly reduced.

Any bumps visible on these “quasi vertical” averaged profiles in the melting layer are considered to be caused by δ . Although the magnitude of δ is expected to be generally lower within the melting layer than in rain, it can be estimated very reliably after azimuthal averaging of the Φ_{DP} data. This result opens a window of opportunity for future work: namely, to examine microphysical properties of the melting layer and to estimate the maximal size of melting snowflakes, which is difficult to estimate using the other radar variables.

4. Observations of backscatter differential phase

Armed with the methods for estimating δ presented above, we can now explore the variability of δ in rain and in the melting layer. Examples of application of the new methods are presented below.

a. Observations of δ in rain

Figure 10 shows the decomposition of the radial profile of measured total differential phase Φ_{DP} into propagation differential phase and δ observed on 22 June 2011 by BoXPOL at elevation 1.5° and azimuth 267° . For the ray considered in Fig. 10, the parameters are $\hat{\alpha} = 0.25$ and $\hat{b} = 0.83$. Note that the raw Φ_{DP} profile shows increased variability at the far ranges with some decreases around range bins 550 and 700 (i.e., at 5.5- and 7-km distance). Such breaks may result in unreliable attenuation correction and negative K_{DP} values when applying a simple moving-average filter and least squares regression.

The procedure includes three steps: First, the system differential phase (around -92° for BoXPOL at that day) is subtracted (the result is shown in Fig. 10 in blue).

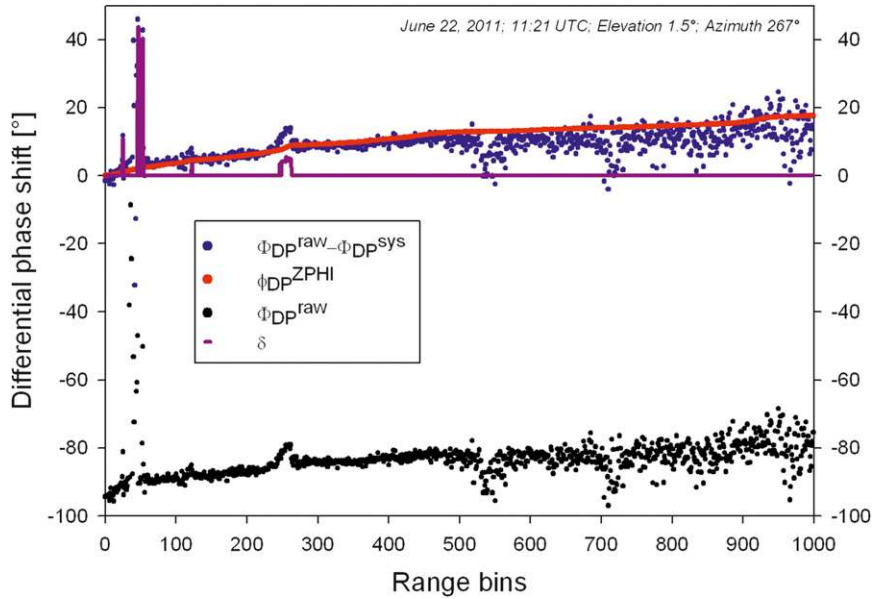


FIG. 10. Total differential phase profile before (black dots) and after (blue dots) subtraction of system differential phase. The estimated differential propagation phase φ_{DP} (red line) as well as the backscatter component δ (purple line) are illustrated for visualizing the δ -detection strategy in pure rain. The example shows the radial profile along azimuth 267° at elevation 1.5° measured on 22 Jun 2011 with BoXPOL.

Second, φ_{DP} is estimated with the ZPHI method. Third, the φ_{DP} profile is subtracted from the measured Φ_{DP} . Differences between Φ_{DP} and φ_{DP} reveal statistical fluctuations, single clutter peaks close to the radar, and δ bumps. The δ bumps at approximately range bin 260 can be identified using $\rho_{hv} > 0.9$ as a criterion for separating δ perturbations from perturbations caused by noise or NBF. In Fig. 10, δ is also plotted separately as the purple line. The two peaks closest to the radar are caused by ground clutter, which will be flagged with an improved clutter filter that is based on the raw I/Q (here, I is the amplitude of the in-phase carrier and Q is the amplitude of the quadrature-phase carrier) data, which we are currently developing.

To demonstrate the reliability of the method, the spatial and temporal continuity of δ estimates are illustrated in Figs. 11 and 12, respectively. Figure 11 shows the BoXPOL observations of total differential phase Φ_{DP} and the estimated differential propagation phase φ_{DP} at azimuth 263° , 265° , and 267° . For all profiles, our method clearly identifies and quantifies δ bumps around range bin 250. The coincidence of this region with increased Z_{DR} (not shown) corroborates the results of our method. Figure 12 shows PPIs of δ estimates from four successive radar scans between 1111 and 1126 UTC, zoomed in on the region of interest. Cells of δ can be clearly identified and consistently tracked over time, which demonstrates the spatial and temporal coherency of the retrieved δ and

attests to the reliability of our estimation method. Our method is, however, less suitable for regions with high K_{DP} ; subtracting the estimated propagation component from the measured differential phase profiles may result in accidental residuals if high gradients of Φ_{DP} prevail.

Figure 13 compares K_{DP} estimates resulting from our method with those derived from the measured Φ_{DP} using a simple moving-average filtering and least squares regression. In the first case, the derivative of the calculated propagation phase over 2 km (20 bins) has been used. In the second case, a moving-average filter over 4 km and an ensuing least squares fit of the radial slope of smoothed differential phase over 2 km has been applied. It is obvious that K_{DP} estimates derived from the measured Φ_{DP} may reveal spurious oscillations caused by unaccounted-for contributions from δ . Negative K_{DP} values in the area around azimuth 315° between range bins 500 and 750 on the right panel of Fig. 13 are caused not by δ but by depressions in the cross-correlation coefficient ρ_{hv} and subsequent nonmonotonic behavior of Φ_{DP} . The ZPHI method, however (see left panel of Fig. 13), represents a more robust strategy to handle such areas of reduced signal-to-noise ratio (i.e., no negative K_{DP} values occur). In addition, note the improved range resolution afforded by the new method. We conclude that our method, which is based on the ZPHI technique, provides reasonably robust estimates of δ and K_{DP} in pure rain areas in which Φ_{DP} does not behave erratically

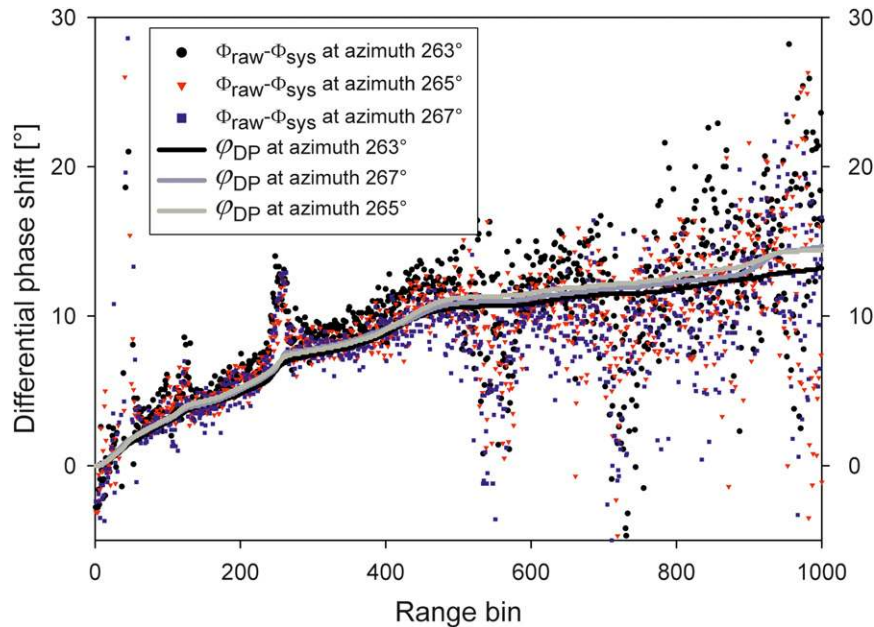


FIG. 11. Raw profiles of total differential phase Φ_{DP} and estimated differential propagation phase ϕ_{DP} at azimuths 263° , 265° , and 267° at 1121 UTC 22 Jun 2011 observed with BoXPOL.

as a result of, for example, NBF effects or low signal-to-noise ratio. This is demonstrated by the spatial and temporal continuity of the δ features and robust K_{DP} estimates.

b. Observations of δ in the melting layer

The polarimetric X-band radar in Jülich, Germany (JuXPOL), scans every 5 min at 37° elevation. Figure 14 shows the azimuthally averaged profiles of Φ_{DP} , Z_{DR} , ρ_{hv} , and Z_H measured at 0450 UTC 24 September 2010 with JuXPOL. The melting layer is clearly identified at around 2.2-km height, showing an increase in Z_H and Z_{DR} and a decrease of ρ_{hv} . The local increase of Φ_{DP} is now almost exclusively attributed to δ . The maximum δ value is about 7.5° .

A similar technique was applied to the data collected with a C-band polarimetric radar in Oklahoma. Figure 15 is an example of azimuthally averaged quasi-vertical profiles of the polarimetric radar variables measured by the C-band University of Oklahoma Polarimetric Radar for Innovations in Meteorology and Engineering (OU-PRIME; Palmer et al. 2011). Again, the melting-layer bright band is clearly observed in the vertical profiles of all four polarimetric radar variables. Owing to OU-PRIME's very high resolution, the average profiles have very low statistical errors (i.e., more samples are averaged to produce the quasi-vertical profiles). In addition, NBF is expected to be negligible at 0.5° beamwidth. The maximal value of δ in this example exceeds 5° . Other scans (not shown) revealed a maximum δ between 5° and 8° . At

S band, the magnitude of δ in the melting layer is expected to be smaller. Figure 16 shows an example from the polarimetric Weather Surveillance Radar-1988 Doppler (WSR-88D) near Seattle, Washington (identified as KATX). Because of the larger beamwidth and smaller number of pulses for each radial, the data are noisier than in the previous example. Nonetheless, the melting-layer signature is clearly seen in each variable. The maximum δ from this case is $\sim 5.5^\circ$. From other scans (not shown), the maximum δ ranged from 3° to 6° , which is lower than the range of values observed at C band as expected.

Figure 17 presents the relative heights of different polarimetric moments and their magnitudes in the melting layer during a stratiform event on 4 December 2011 between 1936 and 2229 UTC observed with BoXPOL at 7° elevation. Strong correlations exist between the radial maxima in azimuth-averaged δ and Z_{DR} (Fig. 17a), the maximum δ and minimum ρ_{hv} (Fig. 17b), and the ρ_{hv} minimum and Z_{DR} maximum (Fig. 17c). Since the strength of the NBF effect should not depend on Z_{DR} or ρ_{hv} , such correlations prove that δ estimates are reliable and that NBF effects are negligible. High values of Z_{DR} and δ combined with low ρ_{hv} usually indicate melting of aggregated and less-rimed snow (e.g., Ryzhkov et al. 2013a,b). The extrema for different moments also occur at different heights, which provides information that is useful for understanding the microphysics of the melting layer. The observations show a δ

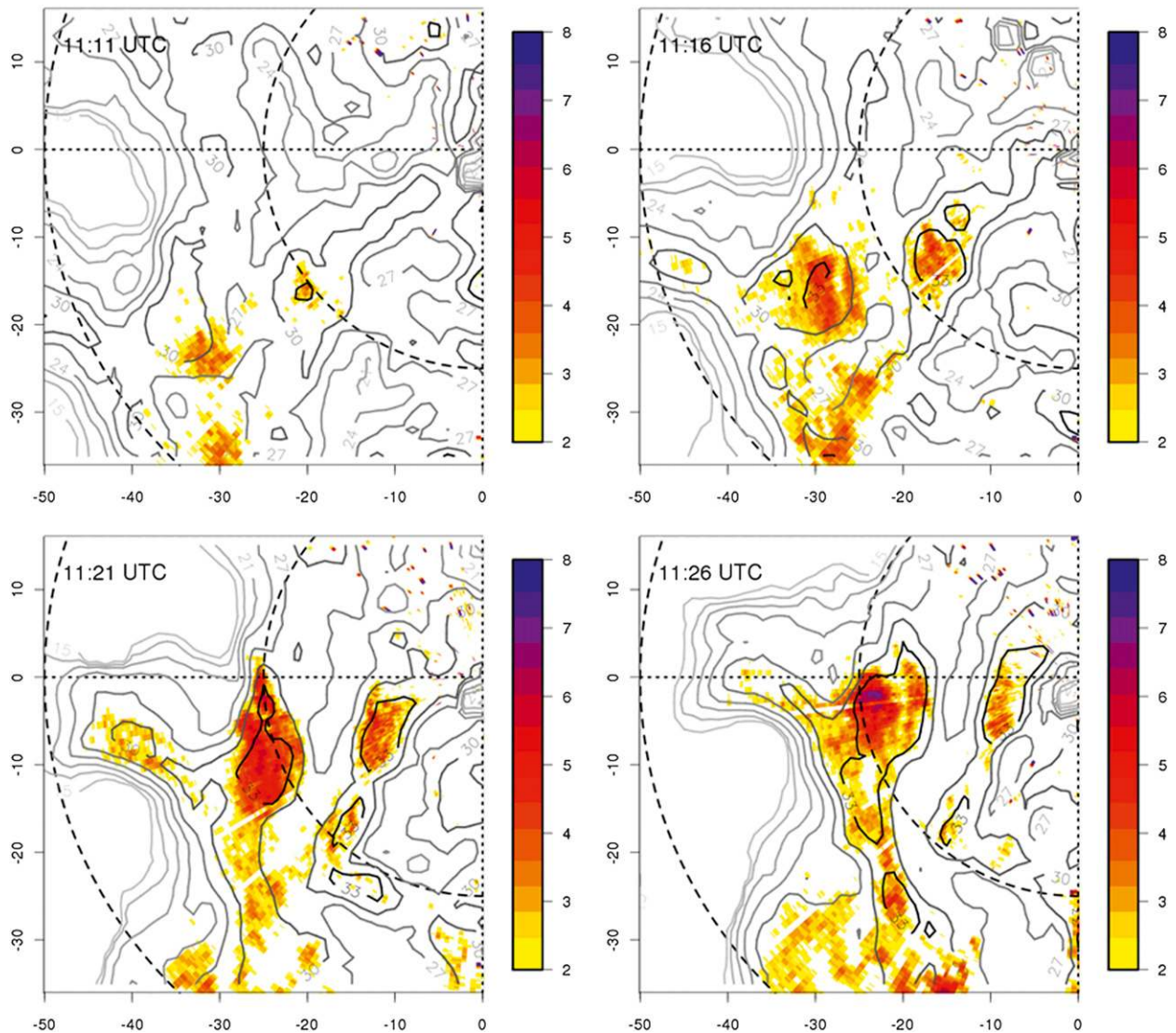


FIG. 12. PPIs of δ generated from observations on 22 Jun 2011 with BoXPOL at four consecutive time steps between 1111 and 1126 UTC. The δ estimates have been smoothed with a moving-average filter over seven bins. Solid lines show contours of horizontal reflectivity Z_H , and dashed lines indicate the 25- and 50-km distances from the radar, respectively.

maximum generally above the ρ_{hv} minimum (Fig. 17d) and the Z_{DR} maximum (Fig. 17e), whereas the relation to the Z_H maximum is not as clear (Fig. 17f). Note that on the basis of simulations the level of Z_H maximum is expected above the ρ_{hv} minimum and δ maximum, whereas the latter are expected at approximately equal height. Such strong correlations between different radar variables—as depicted in Fig. 17—are not seen for all events investigated so far, however. Two events observed with BoXPOL on 11 May and 9 June 2010 show weak or negligible correlation between δ and ρ_{hv} . The δ bumps are broader and the minima in ρ_{hv} are very flat and hard to identify, which possibly hints at a smaller amount of large melting snowflakes or heavily rimed snow.

Berenguer and Zawadzki (2009) report clear correlations between brightband intensity and Z_{DR} near the surface, hinting at big melting snowflakes that create big raindrops. It follows that δ and Z_{DR} measurements and the analysis of their relationship in the melting layer may open a new avenue to parameterize Z – R relationships to be utilized near the ground. For example, in rimed snow, Z_{DR} and δ are lower (both in the melting layer and in the rain below) and the rain rate is higher for a given reflectivity Z_H as compared with unrimed snow (e.g., Ryzhkov et al. 2013b). Thus, rainfall estimation may benefit from the quantification of different polarimetric variables in the melting layer. In object-based approaches to precipitation system analysis from the Lagrangian perspective (Trömel

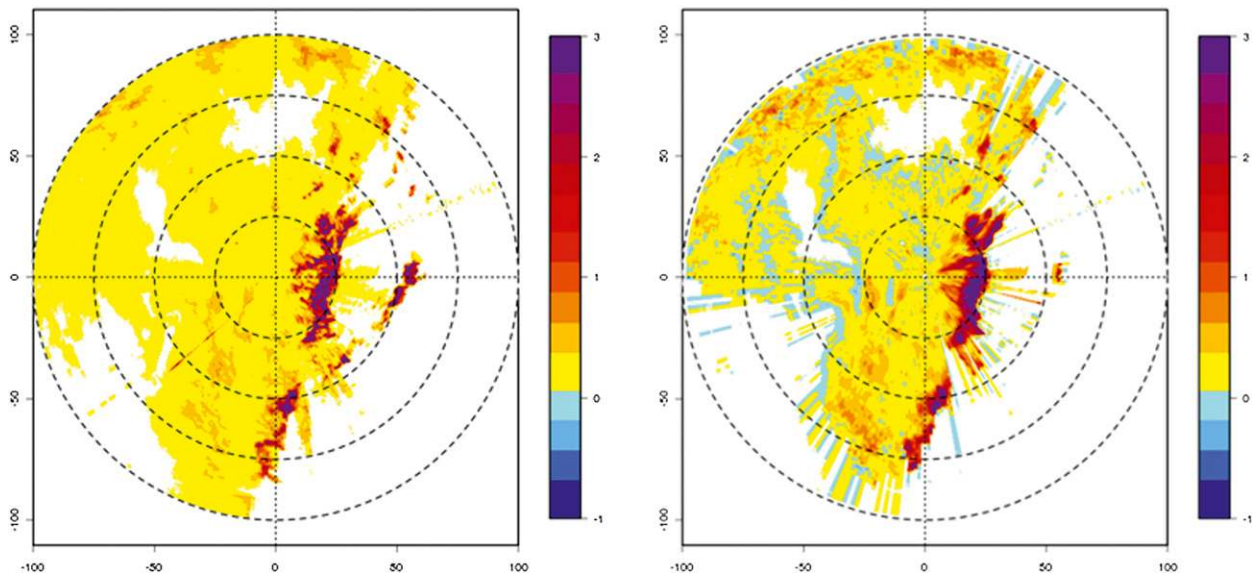


FIG. 13. PPIs of K_{DP} generated from BoXPol observations at 1121 UTC 22 Jun 2011 based on (left) calculated ϕ_{DP} using the method introduced in section 3 and (right) measured Φ_{DP} using moving-average filtering and least squares regression.

et al. 2009; Trömel and Simmer 2012), up to now solely reflectivity-derived descriptors have been used to characterize the intensity of the brightband (Rosenfeld et al. 1995a,b). Since the new polarimetric variable δ is an indicator for the dominant size of rain drops and wet snowflakes and thus microphysical processes, it will allow better characterization of the bright band and the temporal evolution of the system. The full information content and benefit of the melting-layer measurements for precipitation

estimation and understanding the microphysics of precipitation processes has to be further explored, however.

5. Discussion

Because Z_{DR} is affected by differential attenuation and is sometimes biased by miscalibration and radome effects, the strong correlation between Z_{DR} and δ (Fig. 5) is of interest for quantitative precipitation estimation.

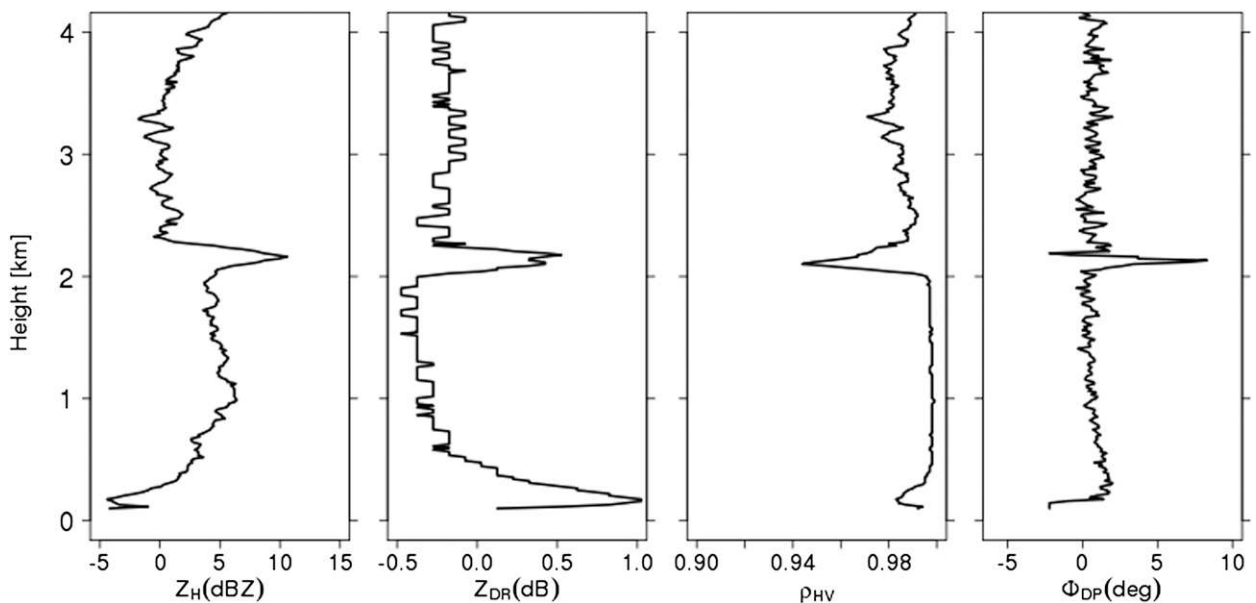


FIG. 14. Example of azimuthally averaged quasi-vertical profiles of Z_H , Z_{DR} , ρ_{HV} , and Φ_{DP} at X band. Data were obtained at 0450 UTC 24 Sep 2010 from the PPI at elevation 37° taken by JuXPol.

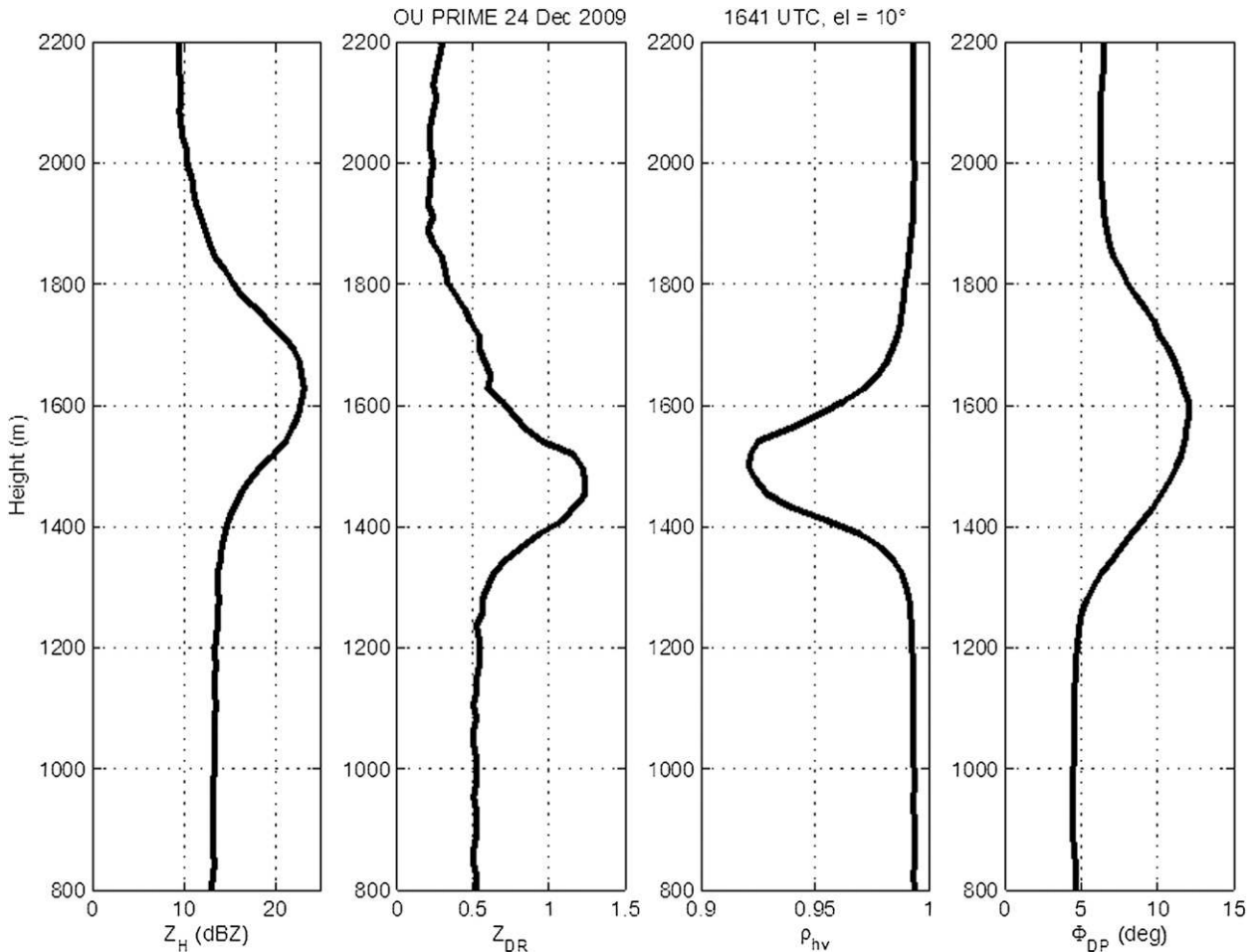


FIG. 15. As in Fig. 14, but at C band and data were obtained at 1641 UTC 24 Dec 2009 from the PPI at 10° elevation taken by OU-PRIME.

Figures 18a and 18b show scatterplots of δ versus the mass-weighted average raindrop diameter D_{mw} at 15°C, simulated using the disdrometer-measured DSDs in Oklahoma and Bonn. In a similar way, Figs. 18c and 18d show scatterplots of Z_{DR} versus D_{mw} . Even though the Z_{DR} – D_{mw} relationship shows less variability, δ also exhibits a relation that could be exploited for better characterizing drop sizes when Z_{DR} is affected by attenuation. Note that, because of its relation to D_{mw} , Z_{DR} is often used to retrieve the slope parameter of the DSD (e.g., Zhang et al. 2001). Figure 18 demonstrates that δ could also be used for such a retrieval—in particular, in the resonance range when the intrinsic Z_{DR} is above ~ 1.2 dB. This may be especially useful at shorter wavelengths (e.g., C and X bands), at which Z_{DR} can be biased by differential attenuation. Because δ is immune to attenuation, it could serve as a proxy for Z_{DR} once Z_{DR} is compromised. On the basis of a polynomial relation, the D_{mw} can be estimated from δ at X band using

$$D_{mw} = a_0 + a_1\delta + a_2\delta^2, \quad (13)$$

where coefficients a_0 , a_1 , and a_2 are functions of temperature as listed in Table 2. They were obtained using simulations that were based on a large DSD dataset in Oklahoma. On average, D_{mw} increases from about 2 to 3.5 mm for δ increasing from 2° to 9°. Hence, the backscatter differential phase at X band can be utilized to quantify mean volume diameters that are larger than 2 mm. Our analysis shows that the fractional root-mean-square error of the $D_{mw}(\delta)$ estimate varies between 15% and 20% for δ within the range 2°–8° for a given temperature. The temperature can be retrieved either from soundings or from the output of numerical weather prediction models. The one of the four $D_{mw}(\delta)$ relations with the closest temperature can be picked to estimate D_{mw} .

The modeled vertical profiles of δ within the melting layer in Fig. 8 agree at least qualitatively with observations. Indeed, both theoretical and observed maxima of δ are

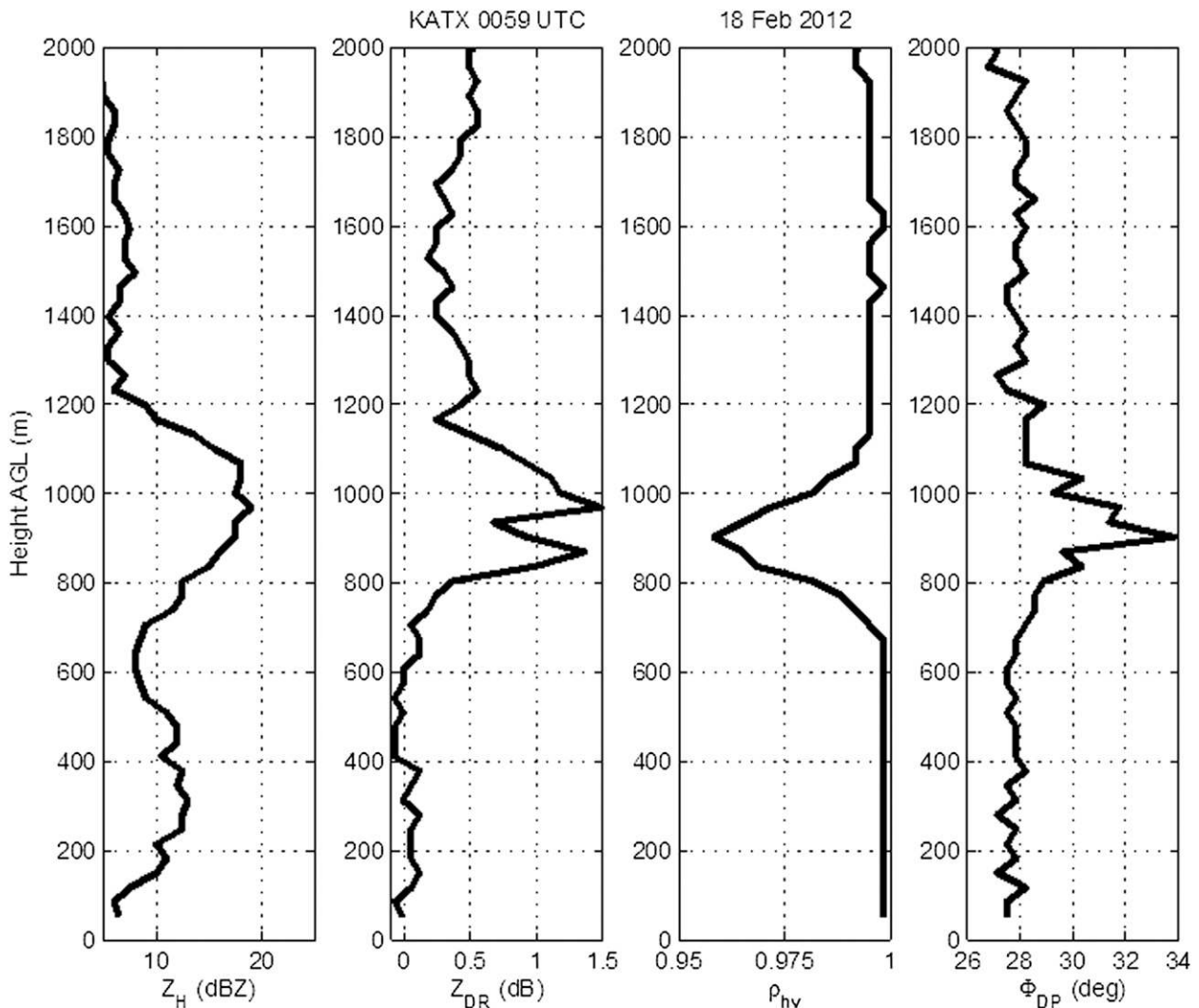


FIG. 16. As in Fig. 14, but at S band and data are from 0059 UTC 18 Feb 2012 from the PPI at 7.5° elevation taken by the KATX polarimetric WSR-88D near Seattle.

approximately at the same heights as the maxima of Z_{DR} and are well below the maxima of Z . The maximal observed values of δ are significantly higher than simulated by the polarimetric model of the melting layer described in section 2, however—especially at S and C bands. We attribute this to the fact that the model does not allow for aggregation of wet snowflakes, which may play an important role in the transformation of the wet-snow spectrum within the melting layer (Barthazy et al. 1998; Goeke and Waldvogel 1998). In situ measurements often indicate that a maximal particle size is attained within the melting layer and not at its top as the model prescribes. Giangrande (2007) and Ryzhkov et al. (2013a) showed that the model yields more realistic values of Z_{DR} and ρ_{hv} (i.e., higher Z_{DR} and lower ρ_{hv}) if aggregation is taken into account. In a similar way, the enhancement

of δ is expected for the same reason, but the corresponding modification of the theoretical model is beyond the scope of this study. Nevertheless, it is important that the availability of reliable measurements of δ provides another physical parameter for the fine tuning and validation of microphysical models of the melting layer.

6. Conclusions

Backscatter differential phase δ is significant for large hydrometeors of resonance size; δ emerges as an important polarimetric variable that should not be ignored in precipitation estimates that are based on K_{DP} at shorter radar wavelengths and as a variable that bears important information about the dominant size of raindrops as well as wet snowflakes in the melting layer. Backscatter

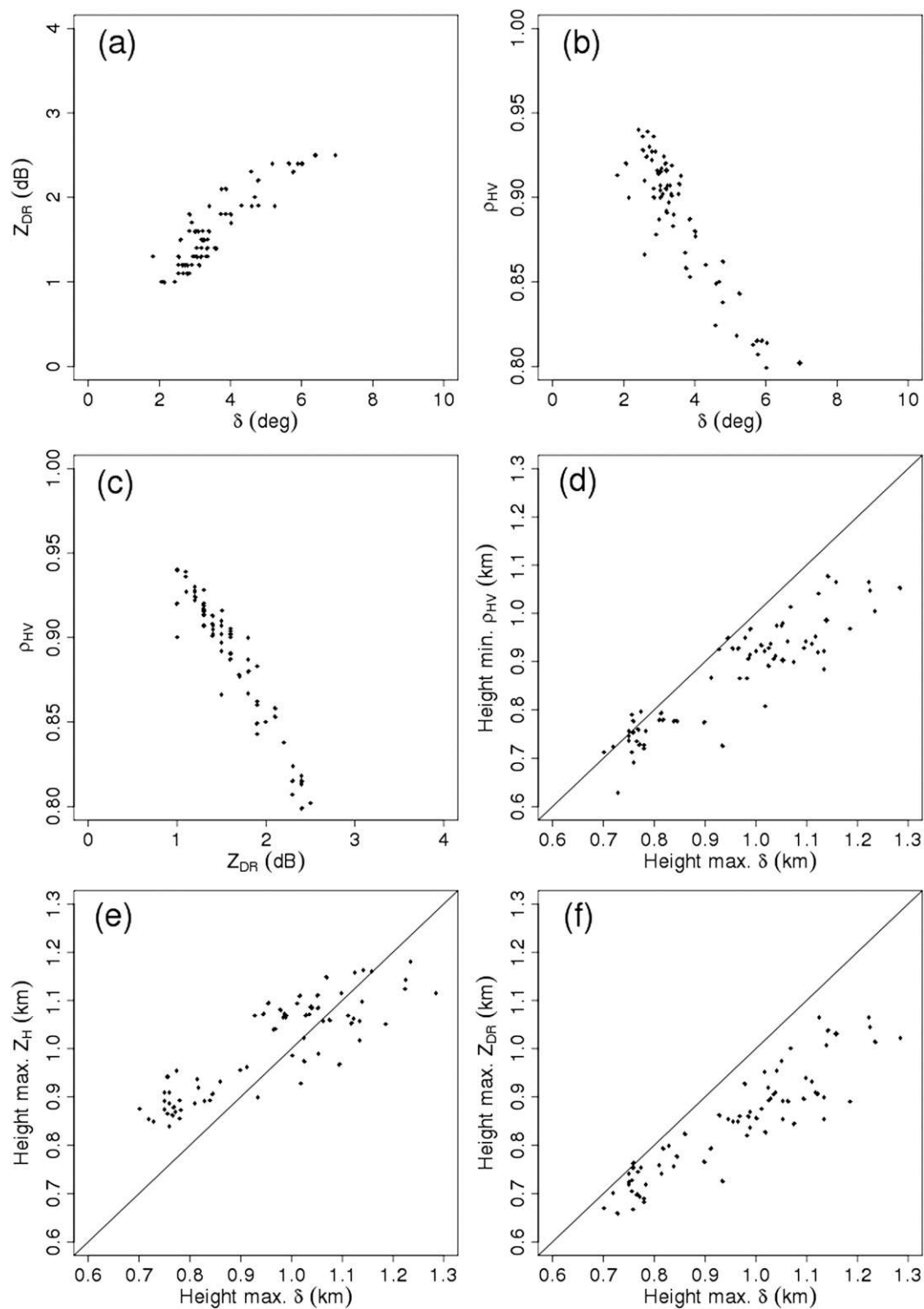


FIG. 17. Relative heights and magnitudes of the extremes of Z_{DR} , ρ_{HV} , and δ in the melting layer observed with BoXPOL at 7° elevation on 4 Dec 2011.

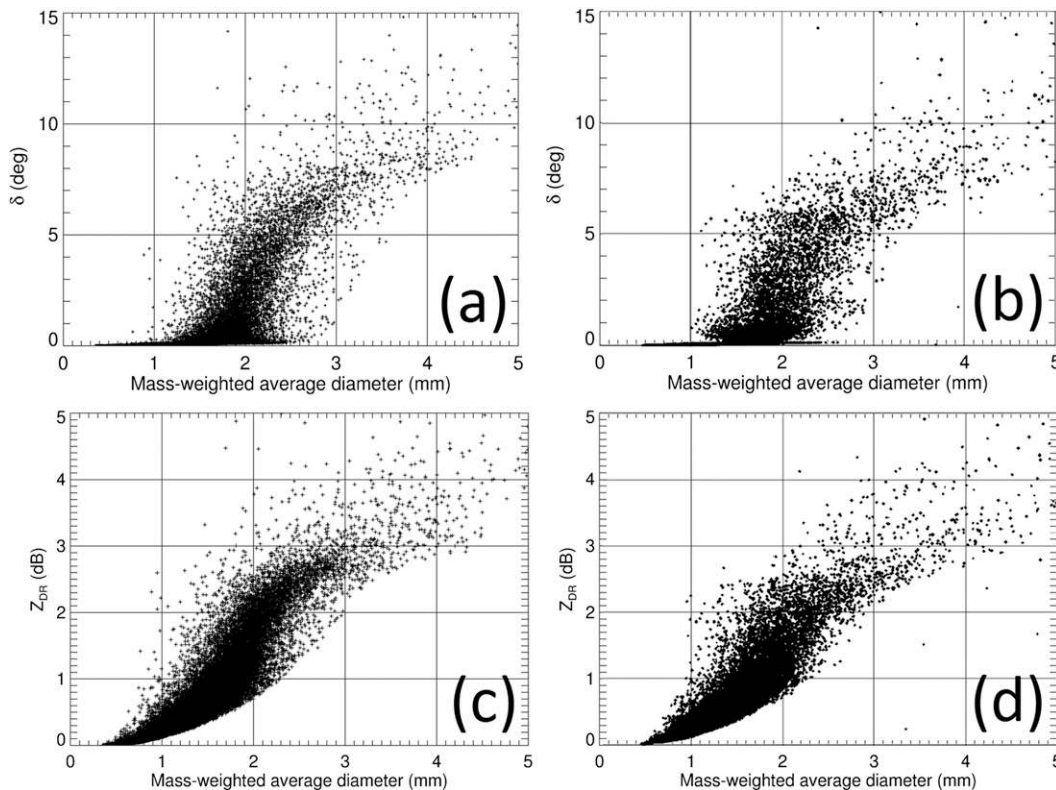


FIG. 18. The (a),(b) δ vs mass-weighted average diameter on the basis of DSD measurements and (c),(d) Z_{DR} vs mass-weighted average on the basis of DSD measurements in (left) Oklahoma and (right) Bonn. Computations are for X band at $T = 15^{\circ}\text{C}$.

differential phase contributes to the total differential phase Φ_{DP} along with the propagation differential phase φ_{DP} . For accurate rainfall estimates using K_{DP} at X band, the contributions from the backscattered and propagation components of Φ_{DP} need to be separated before K_{DP} is estimated from the range derivative of Φ_{DP} .

A new method for estimating δ in pure rain has been suggested. It is based on the ZPHI method and provides reasonably robust estimates of δ and K_{DP} in pure rain where Φ_{DP} is not affected by NBF or low signal-to-noise ratio. Results of δ estimation in rain using polarimetric radars at X band have been presented. One of the possible benefits of using δ is its direct relation to the prevalent size of hydrometeors so that δ can be used for a more accurate retrieval of hydrometeor size distributions. Large disdrometer datasets collected in Oklahoma and Germany indirectly confirm a strong interdependence between backscatter differential phase δ and differential reflectivity Z_{DR} . The overwhelming part of the remaining variability can be related to the temperature of raindrops, whereas the impact of the differences in DSDs seems to be small. Since Z_{DR} is affected by differential attenuation and is sometimes biased by

miscalibration, the strong correlation between Z_{DR} and δ is of interest for quantitative precipitation estimation. The δ and Z_{DR} are differently affected by particle size spectra and can complement each other for particle size distribution retrievals.

For the first time, reliable estimates of δ are obtained within the melting layer of stratiform precipitation at S, C, and X band through azimuthal averaging of radial profiles of Φ_{DP} at high antenna elevations. For such elevations, the impact of nonuniform beam filling seems to be negligibly small and the bumps on the Φ_{DP} profiles are solely attributed to δ . The δ , which is immune to attenuation, partial beam blockage, and radar miscalibration, would complement the information that is routinely available from Z , Z_{DR} , and ρ_{HV} , which are traditionally

TABLE 2. The coefficients in the $D_{mw}(\delta)$ polynomial relation [Eq. (13)].

Temperature ($^{\circ}\text{C}$)	a_0	a_1	a_2
0	1.69	0.174	0.0036
10	1.80	0.052	0.018
20	1.95	-0.085	0.031
30	2.05	-0.142	0.033

used for characterizing microphysical properties of the melting layer. The magnitude of δ can be utilized as an important calibration parameter for the improvement of microphysical models of the melting layer. We advocate for future investigations of δ to explore further the informative content of this underutilized polarimetric variable for microphysics studies as well as quantitative precipitation applications.

Acknowledgments. The research of S. Trömel was carried out in the framework of the Hans-Ertel-Centre for Weather Research (<http://www.herz-tb1.uni-bonn.de/>). This research network of universities, research institutes, and the Deutscher Wetterdienst (DWD) is funded by the BMVBS (Federal Ministry of Transport, Building and Urban Development). We gratefully acknowledge the support by the Terrestrial Environmental Observatories (TERENO) project, funded by the Helmholtz-Gemeinschaft, for providing the JuXPOL observations and the support by the Transregional Collaborative Research Centre 32 (SFB TR 32) funded by the German Research Foundation (DFG) for providing the BoXPOL data. Alexander Ryzhkov and Matthew Kumjian were supported with funding from NOAA/University of Oklahoma Cooperative Agreement NA11OAR4320072 under the U.S. Department of Commerce and from the National Science Foundation (Grant AGS-1143948). Special thanks are extended to Scott Ganson for helping with scattering computations.

REFERENCES

- Aydin, K., V. Giridhar, and Y. Zhao, 1991: Polarimetric C-band radar observables in melting hail: A computational study. Preprints, *25th Int. Conf. on Radar Meteorology*, Paris, France, Amer. Meteor. Soc., 733–736.
- Balakrishnan, N., and D. Zrnić, 1990: Use of polarization to characterize precipitation and discriminate large hail. *J. Atmos. Sci.*, **47**, 1525–1540.
- Barthazy, E., W. Heinrich, and A. Waldvogel, 1998: Size distribution of hydrometeors through the melting layer. *Atmos. Res.*, **47–48**, 193–208.
- Berenguer, M., and I. Zawadzki, 2009: On the relationship between $Z-R$, the bright band intensity and Z_{DR} . Recorded Present., *34th Conf. on Radar Meteorology*, Williamsburg, VA, Amer. Meteor. Soc., 4A.3. [Available online at <https://ams.confex.com/ams/34Radar/webprogram/Paper155482.html>.]
- Borowska, L., D. Zrnić, A. Ryzhkov, P. Zhang, and C. Simmer, 2011: Polarimetric estimates of a one month accumulation of light rain with a 3-cm wavelength radar. *J. Hydrometeorol.*, **12**, 1024–1039.
- Brandes, E. A., G. Zhang, and J. Vivekanandan, 2002: Experiments in rainfall estimation with a polarimetric radar in a subtropical environment. *J. Appl. Meteor.*, **41**, 674–685; Corrigendum, **44**, 186.
- Bringi, V. N., T. D. Keenan, and V. Chandrasekar, 2001: Correcting C-band radar reflectivity and differential reflectivity data for rain attenuation. A self-consistent method with constraints. *IEEE Trans. Geosci. Remote Sens.*, **39**, 1906–1915.
- Cao, Q., G. Zhang, E. Brandes, T. Schuur, A. Ryzhkov, and K. Ikeda, 2008: Analysis of video disdrometer and polarimetric radar data to characterize rain microphysics in Oklahoma. *J. Appl. Meteor. Climatol.*, **47**, 2238–2255.
- Doviak, R. J., and D. S. Zrnić, 1993: *Doppler Radar and Weather Observations*. Academic Press, 562 pp.
- Giangrande, S., 2007: Investigation of polarimetric measurements of rainfall at close and distant ranges. Ph.D. dissertation, University of Oklahoma, 236 pp.
- Goeke, S., and A. Waldvogel, 1998: Studies of snowflake aggregation efficiencies within the melting layer. Preprints, *Conf. on Cloud Physics*, Everett, WA, Amer. Meteor. Soc., 458–461.
- Hubbert, J., and V. N. Bringi, 1995: An iterative filtering technique for the analysis of copolar differential phase and dual-frequency radar measurements. *J. Atmos. Oceanic Technol.*, **12**, 643–648.
- Kumjian, M. R., and A. V. Ryzhkov, 2008: Polarimetric signatures in supercell storms. *J. Appl. Meteor. Climatol.*, **47**, 1940–1961.
- , and —, 2009: Storm-relative helicity revealed from polarimetric radar observations. *J. Atmos. Sci.*, **66**, 667–685.
- , and —, 2012: The impact of size sorting on the polarimetric radar variables. *J. Atmos. Sci.*, **69**, 2042–2060.
- Le Bouar, E., J. Testud, and T. D. Keenan, 2001: Validation of the rain profiling algorithm “ZPHI” from the C-band polarimetric weather radar in Darwin. *J. Atmos. Oceanic Technol.*, **18**, 1819–1837.
- Matrosov, S. Y., R. A. Kropfli, R. F. Reinking, and B. E. Martner, 1999: Prospects for measuring rainfall using propagation differential phase in X- and Ka-radar bands. *J. Appl. Meteor.*, **38**, 766–776.
- , K. A. Clark, B. E. Martner, and A. Tokay, 2002: X-band polarimetric radar measurements of rainfall. *J. Appl. Meteor.*, **41**, 941–952.
- Melnikov, V., 2004: Simultaneous transmission mode of the polarimetric WSR-88D. NOAA/NSSL Rep., 84 pp. [Available online at www.nssl.noaa.gov/publications/wsr88d_reports/SHV_statistics.pdf.]
- Mishchenko, M. I., 2000: Calculation of the amplitude matrix for a nonspherical particle in a fixed orientation. *Appl. Opt.*, **39**, 1026–1031.
- Otto, T., and H. W. J. Russchenberg, 2011: Estimation of specific differential phase and differential backscatter phase from polarimetric weather radar measurements of rain. *IEEE Geosci. Remote Sens. Lett.*, **8**, 988–992.
- Palmer, R. D., and Coauthors, 2011: Observations of the 10 May 2010 tornado outbreak using OU-PRIME: Potential for new science with high-resolution polarimetric radar. *Bull. Amer. Meteor. Soc.*, **92**, 871–891.
- Park, S.-G., V. N. Bringi, V. Chandrasekar, M. Maki, and K. Iwanami, 2005: Correction of radar reflectivity and differential reflectivity for rain attenuation at X band. Part I: Theoretical and empirical basis. *J. Atmos. Oceanic Technol.*, **22**, 1621–1632.
- Rasmussen, R., and A. Heymsfield, 1987: Melting and shedding of graupel and hail. Part I: Model physics. *J. Atmos. Sci.*, **44**, 2754–2763.
- Ray, P., 1972: Broadband complex refractive indices of ice and water. *Appl. Opt.*, **11**, 1836–1844.
- Rosenfeld, D., E. Amitai, and D. B. Wolff, 1995a: Classification of rain regimes by the three-dimensional properties of reflectivity fields. *J. Appl. Meteor.*, **34**, 198–211.

- , —, and —, 1995b: Improved accuracy of radar WPMM estimation rainfall upon application of objective classification criteria. *J. Appl. Meteor.*, **34**, 212–223.
- Ryzhkov, A. V., 2001: Interpretation of polarimetric radar covariance matrix for meteorological scatterers: Theoretical analysis. *J. Atmos. Oceanic Technol.*, **18**, 315–328.
- , 2007: The impact of beam broadening on the quality of radar polarimetric data. *J. Atmos. Oceanic Technol.*, **24**, 729–744.
- , and D. Zrnić, 1998: Beamwidth effects on the differential phase measurements of rain. *J. Atmos. Oceanic Technol.*, **15**, 624–634.
- , M. Pinsky, A. Pokrovsky, and A. Khain, 2011: Polarimetric radar observation operator for a cloud model with spectral microphysics. *J. Appl. Meteor. Climatol.*, **50**, 873–894.
- , M. R. Kumjian, S. M. Ganson, and A. P. Khain, 2013a: Polarimetric radar characteristics of melting hail. Part I: Theoretical simulations using spectral microphysical modeling. *J. Appl. Meteor. Climatol.*, in press, doi:10.1175/JAMC-D-13-073.1.
- , —, —, and P. Zhang, 2013b: Polarimetric radar characteristics of melting hail. Part II: Practical implications. *J. Appl. Meteor. Climatol.*, in press, doi:10.1175/JAMC-D-13-074.1.
- Schneebeli, M., and A. Berne, 2012: An extended Kalman filter framework for polarimetric X-band weather radar data processing. *J. Atmos. Oceanic Technol.*, **29**, 711–730.
- Testud, J., E. Le Bouar, E. Obligis, and M. Ali-Mehenni, 2000: The rain profiling algorithm applied to polarimetric weather radar. *J. Atmos. Oceanic Technol.*, **17**, 332–356.
- Trömel, S., and C. Simmer, 2012: An object-based approach for areal rainfall estimation and validation of atmospheric models. *Meteor. Atmos. Phys.*, **115**, 139–151.
- , —, J. Braun, T. Gerstner, and M. Griebel, 2009: Toward the use of integral radar volume descriptors for quantitative areal precipitation estimation: Results from pseudoradar observations. *J. Atmos. Oceanic Technol.*, **26**, 1798–1813.
- Ulbrich, C., 1983: Natural variations in the analytical form of the raindrop size distribution. *J. Climate Appl. Meteor.*, **22**, 1764–1775.
- Zawadzki, I., W. Szyrmer, C. Bell, and F. Fabry, 2005: Modeling of the melting layer. Part III: The density effect. *J. Atmos. Sci.*, **62**, 3705–3723.
- Zhang, G., J. Vivekanandan, and E. A. Brandes, (2001): A method for estimating rain rate and drop size distribution from polarimetric radar measurements. *IEEE Trans. Geosci. Remote Sens.*, **39**, 830–840.
- Zrnić, D., N. Balakrishnan, C. Ziegler, V. Bringi, K. Aydin, and T. Matejka, 1993: Polarimetric signatures in the stratiform region of a mesoscale convective system. *J. Appl. Meteor.*, **32**, 678–693.